Symmetry breaking of laterally unconstrained flexible filaments in a uniform flow

Kui Liu ,* An-Kang Gao, and Xi-Yun Lu †
Department of Modern Mechanics, University of Science and Technology of China, Hefei, Anhui 230026, People's Republic of China

(Received 2 January 2026; accepted 28 May 2026; published 22 June 2026)

This study numerically investigates the dynamics of flexible filaments which are free to move laterally in a uniform flow. The effects of Reynolds number (Re) and bending stiffness (K) on the flow patterns and filament motion are considered. Results indicate that the filament can achieve spontaneous translation or vibration in most cases due to symmetry breaking, without any external energy input. Five distinct motion modes are identified in the Re–K plane, i.e., static, quasistatic, translational, vibrational, and chaotic modes. The translation Reynolds number (Re_V), which scales with the filament's lateral velocity, and Strouhal number (St), a measure of the vibration frequency, are adopted to quantitatively distinguish these modes. For small K, Re_V is found to follow a simple scaling law with Re. A reduced-order parametrized model is developed that accurately describes the local curvature and equilibrium configuration of the filament. Two key parameters, i.e., the effective bending stiffness (K_{eff}) and effective Reynolds number (Re_{eff}), defined based on the effective relative fluid velocity and the filament's lateral projection length, are introduced, successfully collapsing deformation and force data. Moreover, energy characterization shows fluid kinetic energy conversion rates of up to 15.5% to bending energy and 81.3% to filament kinetic energy. These findings provide insights into the dynamics of flexible bodies in uniform flow.

DOI: 10.1103/5w11-6yc4

I. INTRODUCTION

Spontaneous symmetry breaking is a fundamental phenomenon observed in diverse nonlinear and nonequilibrium systems, including fluid dynamics and biological processes [1]. A classic example in fluid mechanics is the flow past a stationary cylinder, where increasing the Reynolds number induces the phenomenon of symmetry breaking, leading to the formation of the von Kármán vortex street with periodic vortex shedding [2,3]. The concept of symmetry breaking can not only elucidate a variety of intriguing phenomena but also greatly deepen our understanding of fundamental physical principles [4]. Consequently, these issues have long attracted significant scholarly interest [5–9].

The oscillatory motion of an object in a fluid represents a classic problem involving symmetry breaking. For a rigid wing allowed to translate horizontally while undergoing vertical heaving motion in an initially quiescent fluid, Vandenberghe *et al.* [10] demonstrated that spontaneous forward flight occurs when the flapping frequency exceeds a critical threshold, highlighting the essential role of symmetry breaking in thrust production. Numerical simulation by Alben and Shelley [11] identified two key stages in the generation of motion, with flow symmetry first lost due to instability,

*Contact author: lkui@ustc.edu.cn
†Contact author: xlu@ustc.edu.cn

 ©2026 American Physical Society

followed by the interaction between the body and the previously shed vortex generating thrust, which in turn propels the body forward. Subsequent investigations [12–15] further confirmed and extended these findings by examining the effects of body mass, aspect ratio, and flexibility. Benetti Ramos *et al.* [16] performed a fluid–solid Floquet stability analysis on a self-propelled heaving foil, and found that synchronous and asynchronous unstable modes accurately predict the onset of unidirectional and back-and-forth propulsion, respectively. For a self-propelled flexible plate, the symmetry breaking of the wake is also observed, revealing a correlation with the mass ratio [17,18].

In addition to horizontal free cases, symmetry breaking may also occur for an oscillating body tethered in a uniform flow. Under the circumstances, the amplitude-based Strouhal number $St_A = 2Af/U_\infty$ is the key parameter governing the symmetry properties of the wake [19], where U_∞ is the oncoming flow speed, and A and f are the oscillation amplitude and frequency, respectively. Generally, as St_A increases, the von Kármán vortex street and the reversed von Kármán vortex street appear sequentially, and the average velocity profile remains symmetric about the centerline [20,21]. While, as St_A further increases, symmetry breaking of the wake is triggered and a deflected wake is observed [22]. This deflection arises from the formation of dipole structures, whose self-advection is strong enough to decouple from the subsequent vortex [23]. Marais *et al.* [24] indicated that, compared to the rigid case, foil flexibility can enhance thrust and suppress dipole formation, thereby maintaining wake symmetry.

For the aforementioned actively oscillating bodies, continuous energy input is required. In contrast, fixed flexible bodies immersed in a flow, without active driving, may exhibit passive flapping motions [25–29]. For instance, Zhang *et al.* [30] experimentally demonstrated that a flexible filament or flag with a fixed leading edge transitions from a straight configuration to a flapping state as its length increases. This result was further confirmed by the combined experimental and theoretical study of Shelley *et al.* [31], which also revealed a critical flow velocity required to trigger flapping. Numerical studies on two-dimensional flags have complemented these experimental findings, identifying three distinct flag-fluid interaction regimes, i.e., fixed-point, regular flapping, and chaotic flapping regimes, by varying the Reynolds number, mass ratio [32], and bending stiffness [33].

Large-amplitude flapping can also be achieved in an inverted flag configuration due to symmetry breaking, where the flag is clamped at its trailing edge [34–37]. Previous studies have established that, as flexibility increases, an inverted flag in a uniform flow transitions through four distinct dynamical modes: straight, flapping, deflected, and deflected-flapping [38–40]. Notably, in the flapping mode, the flag undergoes vigorous oscillations and large deformations, enabling the system to store substantial kinetic and bending energy. This high energy density makes inverted flags more promising for energy harvesting applications than the leading-edge-clamped flags [41].

However, these conventional configurations, which fix the leading edge, trailing edge, or both [42], impose significant kinematic constraints on the body. A central question, therefore, is how flexible bodies reconfigure and move when granted additional degrees of freedom, a consideration explored in prior studies of horizontally unconstrained flapping wings [10,11]. To address this, we investigate a fluid-structure interaction system wherein a flexible filament is constrained streamwise at both ends but is free to move laterally. The filament is initially straight and oriented perpendicular to a uniform incoming flow, establishing a symmetric initial condition. In contrast to canonical configurations, this setup allows the filament's dynamic response to the fluid to dictate its motion, allowing it to autonomously select a dynamic equilibrium. This autonomy facilitates the emergence of a richer spectrum of passive dynamical modes, providing an ideal paradigm for studying spontaneous symmetry breaking. Note that any ensuing motion, whether translation or vibration, emerges intrinsically from fluid-structure interactions, without external energy input or restrictive kinematic boundary conditions. We systematically characterize the emergent dynamic states resulting from symmetry breaking, quantifying the associated hydrodynamic forces and structural reconfigurations. Energy transfer mechanisms are also analyzed in depth to evaluate the potential for energy conversion with this system.

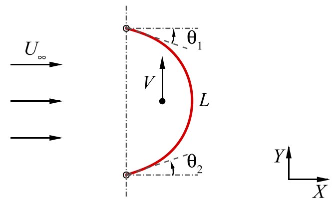

FIG. 1. Schematic diagrams illustrating a flexible filament in a uniform flow. The filament with length L is immersed in a uniform oncoming flow with speed U_∞. The two ends of the filament are fixed in the x-direction and free in the y-direction. Here, V is the lateral velocity of the center-of-mass of the flexible filament, and θ_1 and θ_2 are the angles between the tangent direction of the end points on the windward and leeward sides and the horizontal direction, respectively.

The rest of this paper is organized as follows. The physical problem and mathematical formulation are given in Sec. II. The numerical method and validation are presented in Sec. III. Detailed results are discussed in Sec. IV and concluding remarks are provided in Sec. V.

II. PHYSICAL PROBLEM AND MATHEMATICAL FORMULATION

The schematic diagrams of the flexible filament considered in our study are illustrated in Fig. 1. The filament with length L is immersed in a uniform oncoming flow with speed U_∞. The two ends of the filament are fixed in the x-direction and unconstrained in the y-direction, while other parts of the filament can move freely, facilitated by fluid-structure interactions. Hence, in some cases, due to symmetry breaking, the filament may experience passive lateral motion with a nonzero lateral velocity.

The incompressible Navier-Stokes equations are employed to model and solve the fluid flow,

$$\frac{\partial \boldsymbol{v}}{\partial t} + \boldsymbol{v} \cdot \nabla \boldsymbol{v} = -\frac{1}{\rho}\nabla p + \frac{\mu}{\rho}\nabla^2 \boldsymbol{v} + \boldsymbol{f}_b, \tag{1}$$

$$\nabla \cdot \boldsymbol{v} = 0, \tag{2}$$

where $\boldsymbol{v}$ is the velocity, p is the pressure, ρ is the density of the fluid, μ is the dynamic viscosity, and $\boldsymbol{f}_b$ denotes the Eulerian momentum force acting on the surrounding fluid due to the immersed boundary.

The structural equation is adopted to describe the deformation and motion of the filament [32,43,44],

$$\rho_l \frac{\partial^2 \boldsymbol{X}}{\partial t^2} - \frac{\partial}{\partial s}\left[Eh\left(1 - \left|\frac{\partial \boldsymbol{X}}{\partial s}\right|^{-1}\right)\frac{\partial \boldsymbol{X}}{\partial s}\right] + EI\frac{\partial^4 \boldsymbol{X}}{\partial s^4} = \boldsymbol{f}_s, \tag{3}$$

where s is the Lagrangian coordinate along the plate, ρ_l is the structural linear mass density, $\boldsymbol{X}(s,t) = (X(s,t), Y(s,t))$ is the position vector of the plate, and $\boldsymbol{f}_s$ is the Lagrangian force exerted on the plate by the surrounding fluid. Here, Eh and EI denote the structural stretching rigidity and bending rigidity, respectively.

At $s = 0$, the boundary condition in the x-direction is

$$X(t) = 0, \tag{4}$$

which constrains the x-coordinate of the filament's end point to remain fixed. In the y-direction, the end point is free, necessitating that the y-component of the internal elastic force $\boldsymbol{F}_e$ vanish. From the constitutive relation in Eq. (3), $\boldsymbol{F}_e$ comprises two components: the tension force $\boldsymbol{F}_t = Eh(1 - |\partial \boldsymbol{X}/\partial s|^{-1})\partial \boldsymbol{X}/\partial s$ and the bending force $\boldsymbol{F}_b = -EI\partial^3 \boldsymbol{X}/\partial s^3$. Therefore, projecting these forces onto the y axis yields the boundary condition:

$$-Eh\left(1-\left|\frac{\partial \boldsymbol{X}}{\partial s}\right|^{-1}\right)\frac{\partial Y}{\partial s}+EI\frac{\partial^3 Y}{\partial s^3}=0. \tag{5}$$

Furthermore, at $s=0$, the filament is free to rotate in the plane, which implies a vanishing bending moment, i.e.,

$$\frac{\partial^2 \boldsymbol{X}}{\partial s^2}=0. \tag{6}$$

At the other end point ($s=L$), the same set of conditions applies, reflecting the symmetry in the mechanical constraints at both ends. The initial configuration and velocity of the filament are prescribed as $\boldsymbol{X}(s,0)=(0,s)$ and $\partial \boldsymbol{X}/\partial t(s,0)=(0,0)$, respectively.

In our study, the fluid density ρ, the dynamic viscosity μ, and the dimensional length of the filament L are fixed. To normalize the above equations, the characteristic quantities ρ, L, and $U_{\mathrm{ref}}=\lambda\mu/\rho L$ are chosen, where $\lambda=200$ is a constant. While the specific value of λ may be chosen arbitrarily, this choice merely rescales the magnitude of the normalized results and does not influence the overall trends or conclusions of the study [45]. Note that using the oncoming flow velocity U_∞ as U_{ref} would be inappropriate because U_∞ is not constant. Consequently, the characteristic time is defined as $T_{\mathrm{ref}}=L/U_{\mathrm{ref}}$. Based on dimensional analysis, the following dimensionless governing parameters are introduced: the Reynolds number based on the oncoming flow speed $Re=\rho U_\infty L/\mu$, the mass ratio of the filament to the fluid $M=\rho_l/\rho L$, the stretching stiffness $S=Eh/\rho U_{\mathrm{ref}}^2 L$, and the bending stiffness $K=EI/\rho U_{\mathrm{ref}}^2 L^3$.

III. NUMERICAL METHOD AND VALIDATION

The lattice Boltzmann method (LBM) [46] is adopted to numerically solve the Navier-Stokes equations, while the finite element method (FEM) [47] is implemented to simulate the motion and deformation of the flexible filament. Fluid-structure coupling is achieved through the immersed boundary method (IBM) [43,48], which facilitates bidirectional interaction between the fluid and structural domains. Specifically, the Lagrangian force $\boldsymbol{f}_s$ is computed using a penalty scheme to enforce the no-slip boundary condition, i.e.,

$$\boldsymbol{f}_s=\alpha_1\int_0^t[\boldsymbol{V}_f(s,t')-\boldsymbol{V}_s(s,t')]\mathrm{d}t'+\alpha_2[\boldsymbol{V}_f(s,t)-\boldsymbol{V}_s(s,t)], \tag{7}$$

where α_1 and α_2 are positive penalty coefficients [49–51], $\boldsymbol{V}_s=\partial\boldsymbol{X}/\partial t$ represents the physical velocity of the filament at the Lagrangian points, and $\boldsymbol{V}_f$ denotes the local fluid velocity obtained through interpolation from the Eulerian grid to the Lagrangian points, i.e.,

$$\boldsymbol{V}_f(s,t)=\int \boldsymbol{v}(\boldsymbol{x},t)\delta(\boldsymbol{x}-\boldsymbol{X}(s,t))\mathrm{d}\boldsymbol{x}. \tag{8}$$

The body force $\boldsymbol{f}_b$ on the Eulerian points can be obtained from the Lagrangian force $\boldsymbol{F}_s$ by applying the Dirac δ function,

$$\boldsymbol{f}_b(\boldsymbol{x},t)=-\int \boldsymbol{F}_s(s,t)\delta(\boldsymbol{x}-\boldsymbol{X}(s,t))\mathrm{d}s. \tag{9}$$

In the present study, a four-point regularized δ function is adopted [52,53],

$$\begin{aligned}\delta&=\frac{1}{\Delta x\Delta y}\phi\left(\frac{x}{\Delta x}\right)\phi\left(\frac{y}{\Delta y}\right),\\ \phi(r)&=\begin{cases}(3-2|r|+\sqrt{1+4|r|-4r^2})/8, & |r|<1,\\ (5-2|r|-\sqrt{-7+12|r|-4r^2})/8, & 1\leqslant|r|<2,\\ 0, & |r|\geqslant 2,\end{cases}\end{aligned} \tag{10}$$

where $|r|$ is the distance between the Lagrangian point and the nearby Eulerian grid points.

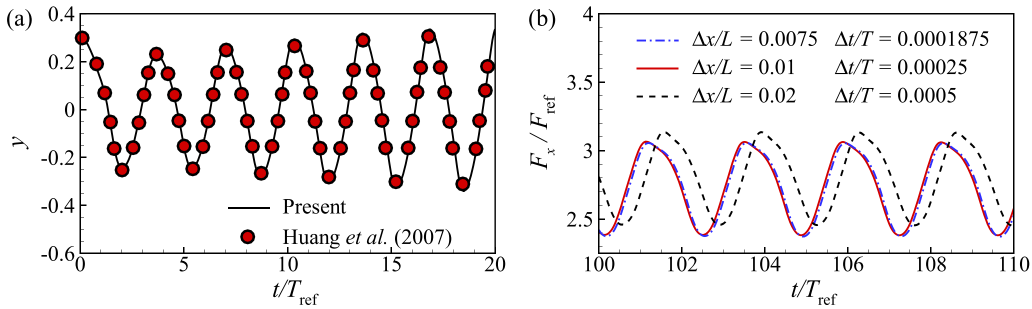

FIG. 2. (a) Validation for the case of a 2D flag in a uniform flow with $Re = 200$, $K = 0.0015$, $M = 1.5$, $S = 1000$, and $Fr = gL/U^2 = 0.5$ [49]. The transverse displacement of the trailing edge of the flag as a function of time is presented. (b) Grid independence and time step independence study for the filament with $Re = 200$, $K = 10^{-4}$, $M = 0.5$, and $S = 10^4$. The streamwise force F_x normalized by $F_{\text{ref}} = (1/2)\rho U_{\text{ref}}^2 L$ as a function of time is presented.

In the simulations, the computational domain for fluid flow is chosen as $[-15L, 25L] \times [-15L, 15L]$ in the x- and y-directions, which is sufficiently large so that the blocking effects of the boundaries are eliminated. Initially, the velocity of the fluid is set to $U_\infty \boldsymbol{e}_x$ throughout the domain, where $\boldsymbol{e}_x$ is the unit vector in the x-direction. A uniform velocity $U_\infty \boldsymbol{e}_x$ is applied at the inlet and the side boundaries, and a convective boundary condition $\partial \boldsymbol{v}/\partial t + U_\infty \partial \boldsymbol{v}/\partial x = \boldsymbol{0}$ is specified at the outlet boundary. Besides, a finite moving computational domain (MCD) is used in the y-direction to allow the filament to move for a sufficiently long time, i.e., as the filament travels one lattice in the y-direction, the computational domain is shifted [44]. In Appendix A, we demonstrate that using an MCD does not affect the kinematic characteristics of the filament.

To validate the numerical method, a 2D flag in a uniform flow is simulated with $Re = 200$, $K = 0.0015$, $M = 1.5$, $S = 1000$, and Froude number $Fr = gL/U^2 = 0.5$ [49]. The transverse displacement of the trailing edge of the flag as a function of time is presented in Fig. 2(a), showing good agreement with the results of Huang *et al.* [49]. In Appendix B, we provide further validation to demonstrate the effectiveness of our algorithm in simulating the free motion of flexible structures. In addition, the numerical strategy employed in this work has been rigorously validated and successfully applied to investigate diverse fluid-structure interaction problems, including the effect of trailing-edge geometry on the propulsive performance of heaving plates [51], the scaling laws governing the self-propulsive performance of flexible plates [54], and the flow-induced reconfiguration of flexible ribbons [45]. Additional detailed numerical validations are available in the corresponding references.

Figure 2(b) shows the results of grid independence and time-step independence for the filament with $Re = 200$, $K = 10^{-4}$, $M = 0.5$, and $S = 10^4$. It is seen that $\Delta x/L = 0.01$ and $\Delta t/T = 0.00025$ are sufficient to achieve accurate results. Hence, in all of the following numerical simulations, $\Delta x/L = 0.01$ and $\Delta t/T = 0.00025$ are adopted.

IV. RESULTS AND DISCUSSION

In the simulations, the mass ratio of the filament to the fluid ($M = 0.5$) and the stretching stiffness ($S = 10^4$) are kept constant. The selection of a sufficiently large S ensures near-inextensibility of the filament [55]. The selected M value aligns with prior studies on flexible bodies in a uniform flow [56–58], where M typically resides in $[0.1, 1]$. Note that the present study does not involve gravity, i.e., the filaments are neutrally buoyant. The remaining two key parameters, namely, the inflow Reynolds number $Re \in [10, 600]$ and the bending stiffness $K \in [10^{-4}, 10^0]$, are variable.

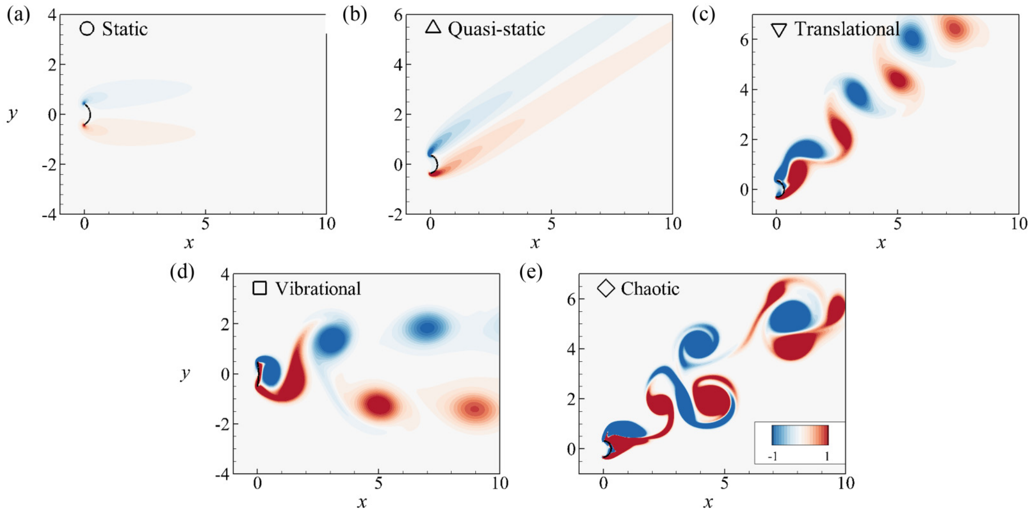

FIG. 3. The instantaneous vorticity contours for the five typical wake patterns of the filament: (a) static ($Re = 20$, $K = 0.0001$), (b) quasistatic ($Re = 40$, $K = 0.0001$), (c) translational ($Re = 100$, $K = 0.0001$), (d) vibrational ($Re = 100$, $K = 0.1$), and (e) chaotic ($Re = 500$, $K = 0.0001$). Animated visualizations for these modes are also provided in the Supplemental movies available at [59].

In the following discussion, the time average of a variable q is defined as

$$\langle q \rangle := \frac{1}{t_1 - t_0} \int_{t_0}^{t_1} q(t)\, \mathrm{d}t. \tag{11}$$

In our computations, the averaging interval $t_1 - t_0$ is selected based on the nature of the quantities under consideration. For periodic quantities, it is set to the fundamental period $T = 1/f_1$, where f_1 is the dominant frequency. For statistically steady (time-invariant) quantities, the interval can be chosen arbitrarily; without loss of generality, it is taken as the characteristic timescale T_{ref} in this study. For quantities exhibiting chaotic behavior, the interval is chosen as $100T_{\mathrm{ref}}$, which is sufficiently large to obtain a statistically converged average.

A. Dynamic states

The emergent dynamic behaviors and corresponding wake patterns of the filament are first systematically examined. Through extensive numerical simulations, five distinct modes are identified, i.e., static, quasistatic, translational, vibrational, and chaotic modes. Figure 3 shows the wake structures of some typical cases for these modes. The subsequent section provides a detailed analysis of their characteristic features.

Figure 3(a) illustrates the instantaneous vorticity contours for the static mode at $Re = 20$ and $K = 0.0001$. In this low-Re regime, the filament exhibits static deformation due to fluid loading. Symmetrical shear layers of opposing vorticity form at the upper and lower edges of the filament, extending downstream in a manner analogous to bluff-body wakes at small Re [58]. When K remains constant at 0.0001 and Re increases to 40, symmetry breaking occurs, leading to a quasistatic mode [Fig. 3(b)]. Under the circumstances, the filament undergoes steady lateral translation at a constant velocity V. Nevertheless, similar to the static mode, the shear layers remain attached to the filament and dissipate further downstream, generating an inclined and stable wake.

Upon further increasing Re to 100 while maintaining $K = 0.0001$ [Fig. 3(c)], the filament exhibits unidirectional translation coupled with vibrational motion, referred to as the translational mode (see the Supplemental movies available at [59]). It is interesting and noteworthy that this

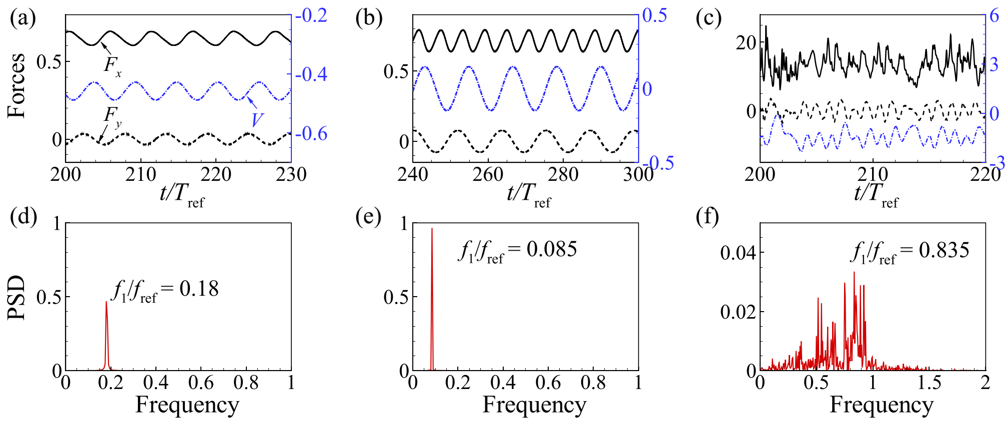

FIG. 4. Time history of the streamwise force F_x, lateral force F_y, and lateral velocity of the center-of-mass V of the filament for (a) $Re = 100$, $K = 0.0001$, (b) $Re = 100$, $K = 0.1$, and (c) $Re = 500$, $K = 0.0001$, corresponding to the translational, vibrational, and chaotic modes, respectively. Panels (d)–(f) are the corresponding power spectrum density (PSD) of the lateral force. The frequency is normalized by $f_{\mathrm{ref}} = U_{\mathrm{ref}}/L$.

translation arises spontaneously from the fluid-structure interaction, without any external energy input. In other words, the filament can extract energy from the surrounding flow to sustain its motion, a behavior analogous to the spontaneous translation of droplets on fibers in a crosswind [60]. Furthermore, the shear layer instability leads to the alternate shedding of counter-rotating vortices, forming an inclined von Kármán vortex street in the wake [Fig. 3(c)]. This vortex shedding is responsible for the pronounced oscillations observed in the filament's hydrodynamic forces and velocity. Note that the filament may translate either upward or downward, depending on the initial perturbations (as detailed in Appendix C). Due to symmetry, these two states are identical in nature. For instance, they share the same magnitude of mean translation velocity (see Fig. 18 in Appendix C).

To further characterize the system dynamics, Fig. 4 presents the temporal evolution of the streamwise force ($F_x = \int_0^L \boldsymbol{f}_s \cdot \boldsymbol{e}_x \mathrm{d}s$), lateral force ($F_y = \int_0^L \boldsymbol{f}_s \cdot \boldsymbol{e}_y \mathrm{d}s$, with $\boldsymbol{e}_y$ being the unit vector in the y-direction), and center-of-mass lateral velocity (V), alongside the power spectral density (PSD) of F_y. As shown in Fig. 4(a), for the translational mode, F_x, F_y, and V oscillate periodically at identical frequencies about their mean values. The PSD of F_y [see Fig. 4(d)] reveals a dominant vibration frequency (f_1), corresponding to the vortex shedding frequency, at $f_1/f_{\mathrm{ref}} = 0.18$ (here, $f_{\mathrm{ref}} = U_{\mathrm{ref}}/L$ is the characteristic frequency). Note that the forces and velocity remain time-invariant in both static and quasistatic modes. Consequently, temporal variations and PSD analyses for these modes are omitted in Fig. 4.

Figure 3(d) depicts the vibrational mode at $Re = 100$ and $K = 0.1$. Here, the filament oscillates about a fixed mean position, as evidenced by a zero time-averaged lateral velocity [see Fig. 4(b)]. The corresponding flow field is marked by a classical von Kármán vortex street (see Fig. 3(d) or the Supplemental movies [59]), which generates periodic hydrodynamic forces on the filament. The PSD of F_y suggests an isolated frequency at $f_1/f_{\mathrm{ref}} = 0.085$ [see Fig. 4(e)], which is half of the oscillation frequency of F_x [see Fig. 4(b)]. These observed characteristics are analogous to the vortex-induced vibration (VIV) of an elastically mounted cylinder [61–64].

At higher Re [e.g., $Re = 500$ and $K = 0.0001$ in Fig. 3(e)], the wake transitions to a disordered state (see the Supplemental movies [59]), termed the chaotic mode. The filament's forces and velocity exhibit aperiodic fluctuations [Fig. 4(c)], accompanied by a broadband PSD spectrum [Fig. 4(f)]. Moreover, the vibrational frequency in this regime increases significantly compared to lower-Re cases, as shown in Fig. 4(f).

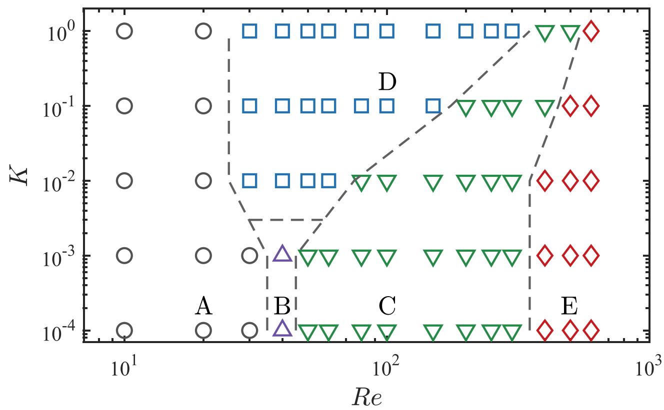

FIG. 5. Phase diagram for the five motion states of the filament. Symbols ○, △, ▽, □, and ♢ represent the static, quasistatic, translational, vibrational, and chaotic modes, respectively. The typical cases in Fig. 3 are labeled as (a)–(e).

The above analysis indicates that these modes can be quantitatively divided by the translational velocity and vibration frequency of the filament, corresponding to two key dimensionless parameters. Specifically, the first is the translation Reynolds number

$$Re_V = \frac{\rho \bar{V} L}{\mu}, \tag{12}$$

where $\bar{V} = |\langle V \rangle|$ is the magnitude of the time-averaged lateral velocity of the filament. The second is the Strouhal number, based on the vibration frequency f_1, inflow speed U_∞, and filament length L [31,45,57]:

$$St = \frac{f_1 L}{U_\infty}, \tag{13}$$

which describes the vibration characteristics of the filament.

Figure 5 displays the phase diagram for the five modes in the Re–K plane, while Fig. 7 illustrates Re_V and St as functions of Re for varying K. For small K (e.g., $K = 10^{-4}$ or 10^{-3}), the static, quasistatic, translational, and chaotic modes emerge sequentially with increasing Re. In contrast, at higher K ($K \geqslant 10^{-2}$), the vibration mode occurs between the static and translational modes (evident in the upper-central region of Fig. 5), and the quasistatic mode is absent. According to Figs. 5 and 7, the characteristics of each mode are summarized as follows.

(i) Static mode: $Re_V = 0$ and $St = 0$, indicating that the filament remains stationary in equilibrium.

(ii) Quasistatic mode: $Re_V > 0$ and $St = 0$, corresponding to pure translation without vibration.

(iii) Vibrational mode: $Re_V = 0$ and $St > 0$, signifying *in situ* oscillatory motion.

(iv) Translational/chaotic modes: $Re_V > 0$ and $St > 0$, reflecting concurrent translation and vibration.

Indeed, a simple quantitative criterion to distinguish between translational and chaotic modes based solely on Re_V and St is lacking. Observing wake structures and PSD distributions serves as a useful auxiliary method, as shown in Figs. 3 and 4. Nevertheless, we would like to propose a feasible quantitative differentiation method in the following.

Note that the PSD of the lateral force signal, denoted by $P(f)$, is normalized such that its discrete summation over the considered positive-frequency range is unity, i.e.,

$$p_i = \frac{P(\hat{f}_i)}{\sum_i P(\hat{f}_i)}, \quad \sum_i p_i = 1, \tag{14}$$

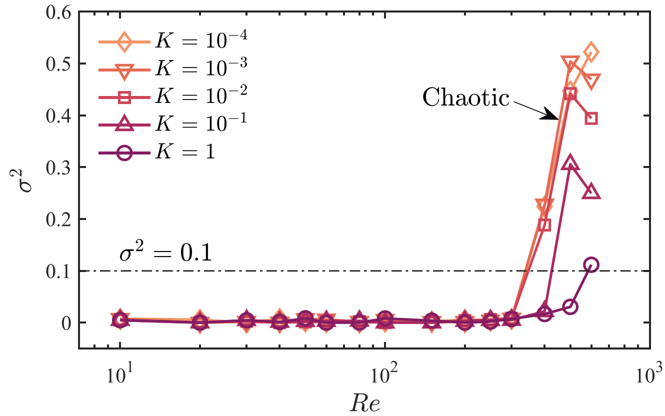

FIG. 6. The variance of the normalized frequency σ^2 as a function of *Re* for different *K*.

where p_i is the normalized PSD and $\hat{f} = f/f_{\mathrm{ref}}$ is the dimensionless frequency. With this normalization, p_i can be interpreted as a probability distribution in frequency space. Hence, the frequency variance σ^2 can be calculated as

$$\sigma^2 = \sum_i (\hat{f}_i - \bar{f})^2 p_i, \tag{15}$$

where $\bar{f} = \sum_i \hat{f}_i p_i$ is the mean frequency. Under this definition, a nearly periodic translational mode gives a sharply concentrated PSD and hence a small value of σ^2, whereas a chaotic mode exhibits a broadband PSD and therefore a much larger value of σ^2. For instance, the translational case depicted in Fig. 4(d) yields $\sigma^2 = 0.0016$, while the chaotic case in Fig. 4(f) gives $\sigma^2 = 0.447$. Therefore, σ^2 provides a quantitative criterion for distinguishing between these two modes.

Figure 6 presents σ^2 as a function of *Re* for different *K*. It is seen that all cases identified as the chaotic mode have σ^2 values clearly larger than 0.1, whereas the translational cases remain below this threshold. This confirms that the threshold $\sigma^2 > 0.1$ is applied consistently in the phase-diagram classification. Accordingly, in the present study, a case is classified as chaotic when $\sigma^2 > 0.1$.

It is also noteworthy that for the translational mode at relatively low *K* (specifically, $K \leqslant 10^{-2}$), Re_V and *Re* obey a simple scaling law, $Re_V \sim Re$, as indicated by the black dashed lines in Fig. 7(a). This relationship arises from a force balance analysis. The lateral force induced by pressure differences, which drives filament motion, scales as $\rho U_\infty^2 L_x$, where L_x represents the filament's

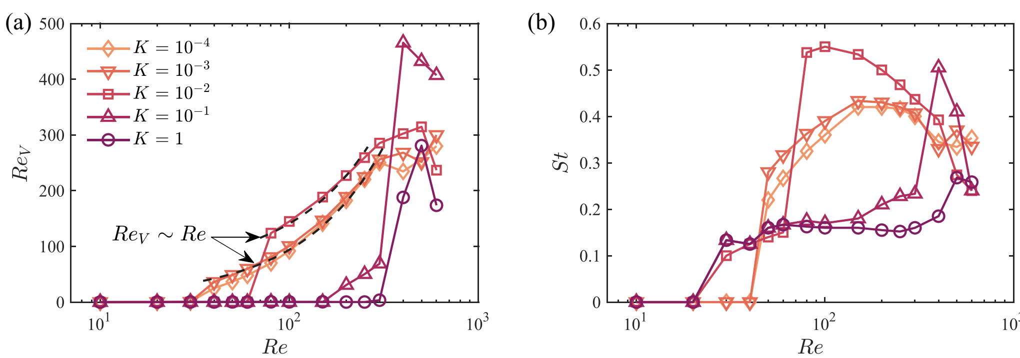

FIG. 7. (a) The translational Reynolds number Re_V, and (b) the Strouhal number *St* for different *K* as functions of *Re*.

streamwise projected length. On the other hand, since the filament resembles a blunt body from a lateral perspective [see the filament in Fig. 3(c) or as detailed in Sec. IV B], the lateral drag acting on the filament scales as $\rho\bar{V}^2L_x$ [65]. Balancing these two forces yields

$$\rho\bar{V}^2L_x \sim \rho U_\infty^2 L_x, \quad \text{or} \quad \bar{V} \sim U_\infty, \tag{16}$$

indicating that the lateral velocity of the filament $\bar{V}$ is proportional to the oncoming flow velocity U_∞. From the definitions of Re_V and Re, (16) can be transformed to

$$Re_V \sim Re, \tag{17}$$

which is highly consistent with the Re_V-scaling observed in Fig. 7(a). Note that, for larger K (e.g., $K = 0.1$ and $Re = 200$), although the filament remains in a translational state, the bending deformation of the filament is relatively small (see Sec. IV B), i.e., the filament no longer resembles a blunt body in the lateral direction. Hence, (16) or (17) is inapplicable to such large-K cases.

B. Reconfiguration and reduced-order parametrized model

In the following, the flow-induced reconfiguration of the filament is further investigated. To quantitatively describe the deformation and force of the filament, the streamwise projected length L_x, lateral projected length L_y, chord-averaged curvature κ_c, and drag F_d are introduced, defined as

$$L_x = \langle X_{\max} - X_{\min}\rangle, \quad L_y = \langle Y_{\max} - Y_{\min}\rangle,$$
$$\kappa_c = \left\langle \frac{1}{L}\int_0^L \kappa\,\mathrm{d}s \right\rangle, \quad F_d = \langle F_x\rangle, \tag{18}$$

where $X_{\max}$ ($Y_{\max}$) and $X_{\min}$ ($Y_{\min}$) are the maximum and minimum streamwise (lateral) coordinates on the filament, respectively, and κ is the local curvature.

Figure 8 illustrates equilibrium configurations for varying Re and K (red solid lines). For a fixed K, increasing flow velocity (i.e., Re) enhances the fluid load on the filament, inducing pronounced deformation (see Fig. 8). Consequently, L_x, κ_c, and F_d exhibit monotonic increases with Re, while L_y progressively decreases, as demonstrated in Fig. 9. These results align with the main characteristics of the reconstruction of flexible bodies in flow [66–69]. With increasing K, the filament becomes stiffer and deforms less, which leads to a decrease in L_x and κ_c and an increase in L_y [see Figs. 9(a)–9(c)]. Besides, F_d approximately follows Re^2-scaling [see dashed line in Fig. 9(d)], which conforms to classical bluff-body theory [65,70,71]. Nevertheless, the data in Fig. 9 lack satisfactory collapse. This limitation will be addressed in Sec. IV C.

It is also noted that the shapes of the filaments vary greatly under different parameters (see Fig. 8). Specifically, at low values of K [e.g., $K = 10^{-4}$ and $Re \geqslant 150$ in Figs. 8(d1)–8(f1)], the filament approximates a circular arc, whereas high K and low Re [e.g., $K = 1$ and $Re \leqslant 80$ in Figs. 8(a3)–8(c3)] produce nearly rectilinear profiles. To describe these shapes uniformly and to gain further insight into the reconfiguration mechanism, a reduced-order parametrized model for the filament is subsequently developed.

According to the force decomposition results in Appendix D, two key assumptions can be made: first, the normal force f_n is approximately evenly distributed along the filament, i.e., $f_n \approx C$; second, the tangential force f_τ is almost negligible, i.e., $f_\tau \approx 0$. Therefore, balancing the local normal force, tension, and bending force yields [72]

$$EI\frac{\partial^2\kappa}{\partial s^2} = T_s\kappa - f_n, \tag{19}$$

where T_s represents the filament tension. Here, T_s can be approximated as a constant along the filament, since $\mathrm{d}T_s/\mathrm{d}s = f_\tau \approx 0$. By scaling space with L, (19) can be normalized as

$$\frac{\partial^2\hat{\kappa}}{\partial\hat{s}^2} = \Pi_1\hat{\kappa} - \Pi_2, \tag{20}$$

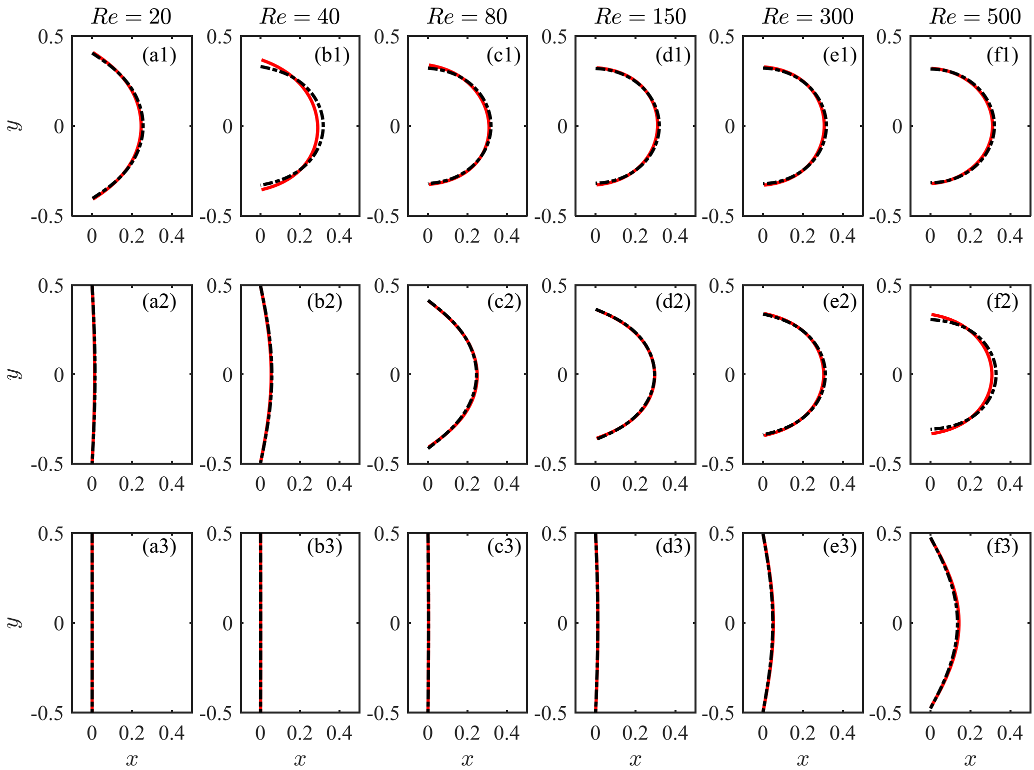

FIG. 8. The equilibrium configurations of the filament for various Re and K. The red solid lines and black dash-dotted lines represent the numerical results and reduced-order model results given by (23), respectively. The rows correspond to $K = 10^{-4}$, 10^{-2}, and 1, from top to bottom. The columns correspond to $Re = 20$, 40, 80, 150, 300, and 500, from left to right.

where $\hat{\kappa} = \kappa L$ and $\hat{s} = s/L$ denote the dimensionless local curvature and dimensionless curvilinear coordinate, respectively. It is worth noting that two dimensionless governing parameters emerge from the scaling, i.e., the ratio of tension to bending force $\Pi_1 = \frac{T_s}{EI/L^2}$ and the ratio of normal force to bending force $\Pi_2 = \frac{f_n L}{EI/L^2}$. These two parameters play a decisive role in determining the equilibrium shape of the filament. Indeed, Π_1 and Π_2 are extracted from numerical simulations rather than *a priori* quantities. Specifically, the tension is calculated using $T_s = Eh(|\frac{\partial \boldsymbol{X}}{\partial s}| - 1)$, while the normal force is obtained via force decomposition, as detailed in Appendix D.

Considering the boundary conditions at the filament ends, namely, $\hat{\kappa} = 0$ at $\hat{s} = 0$ and 1, the analytical solution of (20) is

$$\hat{\kappa}(\hat{s}) = \frac{\Pi_2}{\Pi_1}\left\{1 - \cosh\left[\frac{1}{2}\sqrt{\Pi_1}(2\hat{s} - 1)\right]\operatorname{sech}\left(\frac{\sqrt{\Pi_1}}{2}\right)\right\}, \tag{21}$$

which describes the local curvature of the filament.

Next, we will further consider the filament's shape. As shown in Fig. 8, the filament is nearly symmetric about the horizontal centerline, resulting in a vertical tangent at its midpoint. This corresponds to a local inclination angle $\theta = \pi/2$ at $\hat{s} = 1/2$, which simplifies subsequent shape calculations. Exploiting symmetry, we restrict the analysis to the lower half-domain, i.e., $\hat{s} \in [1/2, 1]$, with the midpoint fixed at (0,0) without loss of generality. The local inclination angle for this

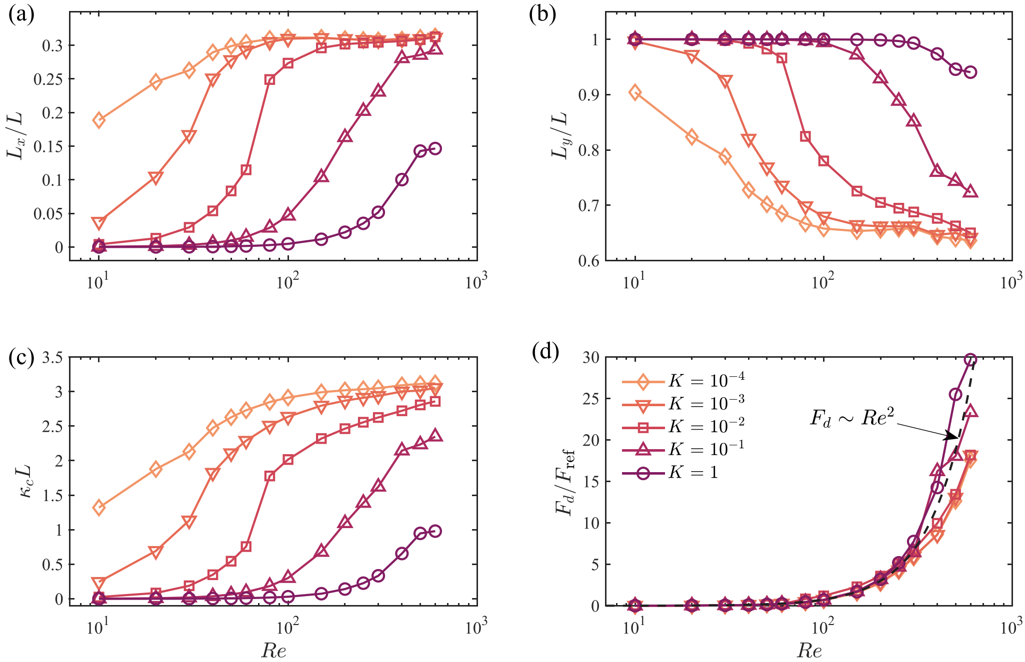

FIG. 9. The normalized time-averaged (a) streamwise projected length L_x, (b) lateral projected length L_y, (c) chord-averaged curvature κ_c, and (d) drag F_d of the filament as functions of Re for various K.

segment is given by

$$\theta(\hat{s}) = \frac{\pi}{2} - \int_{1/2}^{\hat{s}} \hat{\kappa}\,\mathrm{d}\hat{s}, \quad \hat{s} \in [1/2, 1]. \tag{22}$$

Consequently, the local coordinates are obtained as

$$x(\hat{s}) = -\int_{1/2}^{\hat{s}} \cos\theta\,\mathrm{d}\hat{s}, \quad y(\hat{s}) = -\int_{1/2}^{\hat{s}} \sin\theta\,\mathrm{d}\hat{s}, \quad \hat{s} \in [1/2, 1]. \tag{23}$$

The coordinates of the upper half (i.e., $\hat{s} \in [0, 1/2]$) follow directly from symmetry, thus fully determining the shape of the entire filament.

To validate the preceding analysis, Fig. 10 displays the distribution of $\hat{\kappa}$ along the filament for diverse Re and K values, with reduced-order model results from (21) indicated by black dash-dotted lines. The equilibrium filament configurations derived from (22) and (23) are depicted in Fig. 8 (see the black dash-dotted lines). Close agreement between reduced-order model and numerical results for the cases with various parameters is observed (see Figs. 8 and 10), which confirms the model's capability to accurately characterize both local curvature and equilibrium filament configurations.

Note that an interesting implication can be drawn from (21). When K is low and Re is high (e.g., $K = 10^{-4}$ and $Re > 100$), bending forces become negligible compared to tension and normal forces, leading to $\Pi_1 \to \infty$. Under these conditions, the second term in the curly brackets of (21) approaches zero, i.e.,

$$\cosh\left[\frac{1}{2}\sqrt{\Pi_1}(2\hat{s} - 1)\right] \operatorname{sech}\left(\frac{\sqrt{\Pi_1}}{2}\right) \to 0, \quad \hat{s} \in (0, 1). \tag{24}$$

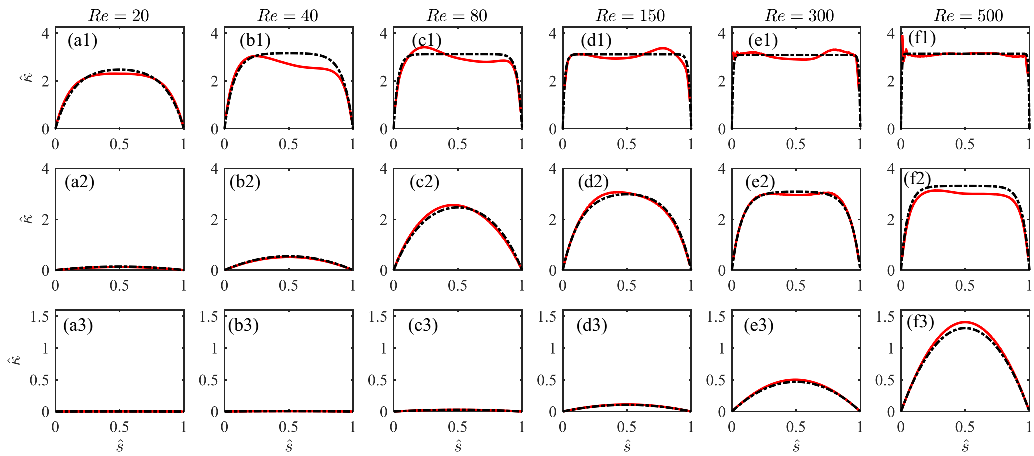

FIG. 10. The dimensionless local curvature $\hat{\kappa}$ along the filament for various Re and K. The red solid lines and black dash-dotted lines represent the numerical results and reduced-order model results given by (21), respectively. For the first, second, and third rows, $K = 10^{-4}$, 10^{-2} and 1, respectively. From left to right, the Re values for each column are 20, 40, 80, 150, 300, and 500, respectively.

Consequently,

$$\hat{\kappa}(\hat{s}) = \frac{\Pi_2}{\Pi_1} = \frac{f_n L}{T_s} = C, \tag{25}$$

meaning constant local curvature along the filament and a circular-arc filament profile. This result is corroborated by Figs. 10(d1)–10(f1), where $\hat{\kappa}$ remains nearly uniform away from the end points. The corresponding equilibrium configurations of the filaments indeed resemble perfect circular arcs [see Figs. 8(d1)–8(f1)].

In addition, for cases with large K, the bending force dominates over the tension, resulting in $\Pi_1 \to 0$. Therefore, (20) reduces to

$$\frac{\partial^2 \hat{\kappa}}{\partial \hat{s}^2} = -\Pi_2. \tag{26}$$

This implies a parabolic distribution (concave downward) for $\hat{\kappa}$ along the filament, a profile that closely matches the observations from Figs. 10(d3)–10(f3). As Re decreases, the curvature gradient diminishes, causing the parabolic profile to flatten and approach a uniform distribution (i.e., $\hat{\kappa} \approx 0$), as illustrated in Figs. 10(a3)–10(c3).

In the above analysis, the filament is assumed to be symmetric about the horizontal centerline. However, this assumption is not strictly valid, since the symmetry of the filament is not so perfect. As depicted in Fig. 10, significant asymmetry in local curvature κ is observed near the two ends of the filament under certain conditions. For example, for the case with $K = 10^{-4}$ and $Re = 80$ in Fig. 10(c1), κ near $\hat{s} = 0$ is relatively larger than that near $\hat{s} = 1$. This curvature asymmetry is a direct manifestation of symmetry breaking in the system, which ultimately leads to lateral translation of the filament.

The asymmetry of local curvature at the two end points also implies a difference in corresponding local inclination angles, denoted as $\theta_1 - \theta_2$, where θ_1 (θ_2) is the angle between the tangent direction of the end point on the windward (leeward) side and the horizontal direction (see Fig. 1). Figure 11 presents $\theta_1 - \theta_2$ as functions of Re for various K. It is seen that, when the filament undergoes lateral translation (i.e., the quasistatic and translational modes), $\theta_1 - \theta_2 < 0$ (see the blue symbols at moderate Re in Fig. 11). In other words, the local inclination angle of the end point on the windward side is smaller than that on the leeward side. This geometric asymmetry may initially

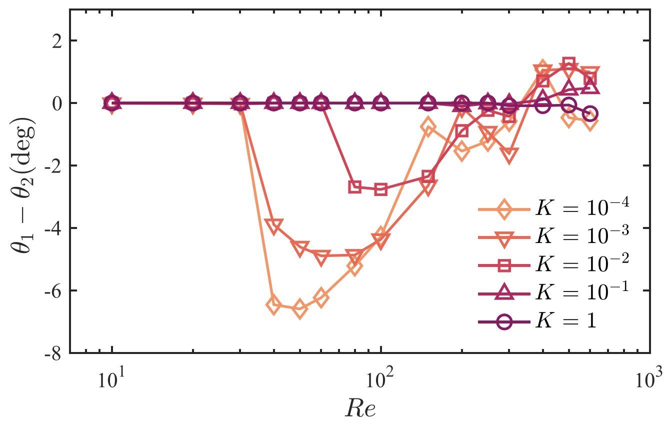

FIG. 11. The difference of the angles between the tangent direction of the end points on the windward and leeward sides and the horizontal direction $\theta_1 - \theta_2$.

result in nonzero lateral forces, which contribute to lateral translation. In contrast, for both the static and vibrational modes, $\theta_1 - \theta_2 = 0$ (see the red symbols for $Re < 200$ in Fig. 11), which reflects a highly symmetric filament shape and accounts for the absence of net lateral displacement.

C. Rescaling

In Sec. IV B, the deformation and force data of the filament are presented to quantitatively characterize the reconfiguration of the filaments. Nevertheless, the datasets exhibit substantial scatter and fail to collapse effectively (see Fig. 9). This obstructs rigorous analysis of the dynamic characteristics in the fluid-structure system and the identification of underlying physical mechanisms. Therefore, to achieve unified data collapse and possible scalings, the introduction of revised scaling parameters is required.

It is worth noting that the fluid force (F_f) and the bending force (F_b) are the two main forces involved in our fluid-structure system, which play a key role in the dynamic characteristics of the filaments. Typically, F_f and F_b can be scaled as $\rho U_\infty^2 L$ and EI/L^2, respectively [73]. However, the filament's lateral translation results in an effective relative fluid velocity $U_{\text{eff}} = \sqrt{U_\infty^2 + \bar{V}^2}$. Similarly, substantial bending deformation leads to an effective length of the filament interacting with the fluid $L_{\text{eff}} = L_y$. Adopting U_{eff} and L_{eff} as characteristic quantities gives $F_f \sim \rho U_{\text{eff}}^2 L_{\text{eff}} = \rho(U_\infty^2 + \bar{V}^2)L_y$ and $F_b \sim EI/L_{\text{eff}}^2 = EI/L_y^2$. Hence, the effective bending stiffness of the filament can be defined as the ratio of these two forces, i.e.,

$$K_{\text{eff}} = \frac{EI}{\rho U_{\text{eff}}^2 L_{\text{eff}}^3} = \frac{EI}{\rho\left(U_\infty^2 + \bar{V}^2\right)L_y^3}. \tag{27}$$

Furthermore, the effective Reynolds number is introduced:

$$Re_{\text{eff}} = \frac{\rho U_{\text{eff}} L_{\text{eff}}}{\mu} = \frac{\rho\sqrt{U_\infty^2 + \bar{V}^2}L_y}{\mu}. \tag{28}$$

All data on filament deformation and force from Fig. 9 are replotted in Fig. 12 against the new scaling parameters (K_{eff} and Re_{eff}). Remarkably, the data collapse well under this scaling, in contrast to the scattered distribution observed in Fig. 9. Besides, for small K_{eff}, $L_x/L \approx 1/\pi$, $L_y/L \approx 2/\pi$, and $\kappa L \approx \pi$ [see Figs. 12(a)–12(c)], corresponding to the radius, diameter, and curvature of a semicircle of unit circumference, respectively. This is consistent with the near-perfect semicircular equilibrium shapes observed for low-stiffness filaments in Figs. 8(d1)–8(f1). Conversely, for large K_{eff}, we find $L_x/L \approx 0$, $L_y/L \approx 1$, and $\kappa L \approx 0$ [see Figs. 12(a)–12(c)], owing to negligible filament

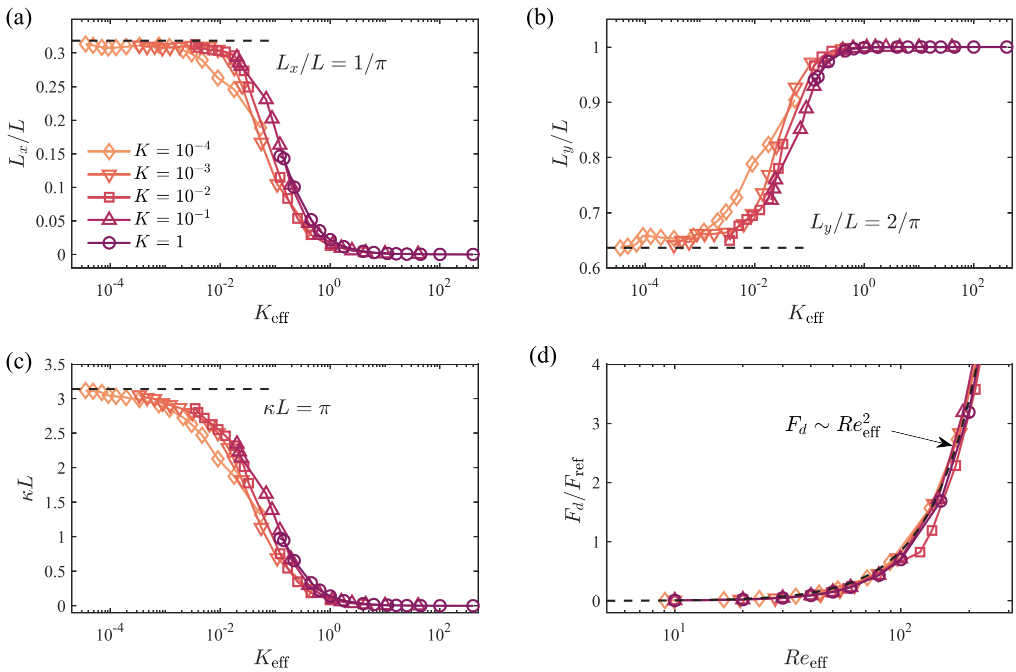

FIG. 12. The normalized time-averaged (a) streamwise projected length $\hat{L}_x$, (b) lateral projected length $\hat{L}_y$, and (c) chord-averaged curvature $\hat{\kappa}_c$ as functions of K_{eff}, and (d) drag $\hat{F}_d$ as functions of Re_{eff} for various K.

deformation, which preserves a straight configuration [see Figs. 8(a3)–8(c3)]. Additionally, F_d follows the Re_{eff}^2-scaling well [see Fig. 12(d)], demonstrating that the drag is proportional to the square of the effective velocity U_{eff} rather than U_∞.

D. Energy conversion

As discussed, a flexible filament with lateral freedom in a uniform flow can undergo significant bending deformation and, under certain conditions, generate sustained lateral motion, which can be measured by the bending energy E_b and the translational kinetic energy E_k, respectively. Specifically, these two quantities are defined as

$$E_b = \left\langle \int_0^L \frac{EI}{2}\kappa^2 \mathrm{d}s \right\rangle, \quad E_k = \frac{1}{2}m\bar{V}^2, \tag{29}$$

respectively, where $m = \rho_l L$ is the dimensional mass of the filament. Figure 13 shows E_b and E_k, normalized by the characteristic energy $E_{\text{ref}} = \rho U_{\text{ref}}^2 L^2$, as functions of Re for various K. For small K, E_b is comparatively larger at low Re due to larger deformation (see Fig. 8). As Re increases, a simple scaling law is robustly satisfied between E_b and Re, namely, $E_b \sim Re^4$ [see Fig. 13(a)], indicating a rapidly growing form of E_b. At high Re, filament deformation shows a negligible increase with further Re augmentation (see Fig. 8), leading E_b to asymptotically approach a plateau [see Fig. 13(a)]. Under the circumstances, E_b depends principally on the flexibility of the filament and increases monotonically with K [see Fig. 13(a)]. For E_k presented in Fig. 13(b), the variation aligns closely with Re_V shown in Fig. 7(a), since $E_k \sim \bar{V}^2 \sim Re_V^2$.

To further evaluate the energy characteristics of the system, two key parameters are introduced: the conversion ratios from fluid kinetic energy to bending energy R_b and to filament translational

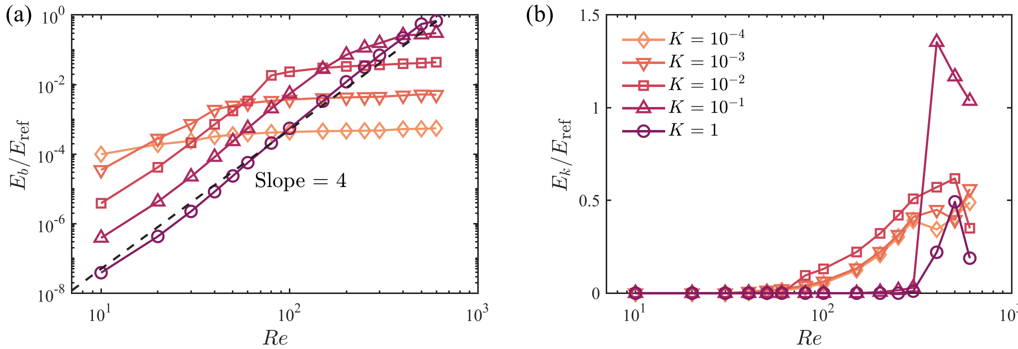

FIG. 13. The normalized time-averaged (a) bending energy E_b, and (b) translational kinetic energy E_k of the filaments as functions of Re for various K. The energy is normalized by $E_{\mathrm{ref}} = \rho U_{\mathrm{ref}}^2 L^2$.

kinetic energy R_k, defined as

$$R_b = \frac{E_b}{(1/2)\rho U_\infty^3 T (L_y + \bar{V}T)}, \quad R_k = \frac{E_k}{(1/2)\rho U_\infty^3 T (L_y + \bar{V}T)}. \tag{30}$$

The denominator in Eq. (30) represents the kinetic energy of the fluid that interacts with the filament over one cycle [38], as illustrated in Fig. 14. Over a single cycle period T, the filament translates laterally by a distance $\bar{V}T$. Consequently, the total length swept by the filament in the lateral direction is $L_y + \bar{V}T$. Simultaneously, a free fluid parcel travels a horizontal distance $U_\infty T$. The area of the fluid that interacts with the filament is therefore $A_f = U_\infty T(L_y + \bar{V}T)$. The corresponding kinetic energy of this fluid volume is $E_{k,f} = \frac{1}{2}\rho U_\infty^2 A_f = \frac{1}{2}\rho U_\infty^3 T(L_y + \bar{V}T)$. Based on this formulation, the two conversion ratios defined in Eq. (30) are readily obtained. The quantities R_b and R_k should therefore be interpreted as estimated energy-conversion ratios normalized by the kinetic energy of the swept fluid, rather than as rigorous energy-conversion efficiencies obtained from a control-volume energy budget.

The derivation presented above implicitly assumes a periodic filament motion. However, this framework can be extended to nonperiodic motion modes. For the chaotic mode, an effective period T is defined based on the dominant frequency f_1, which corresponds to the peak in the PSD,

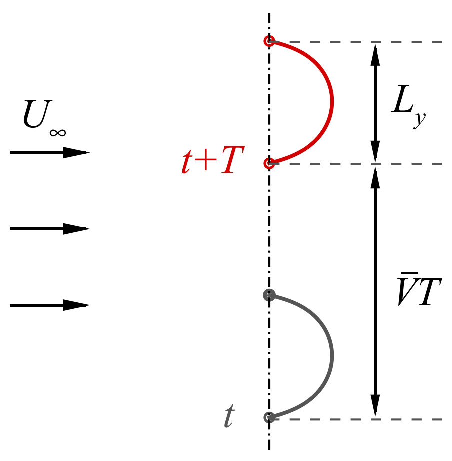

FIG. 14. Schematic diagram of the lateral translation of the filament within one cycle T. From t to $t + T$, the filament moves upward.

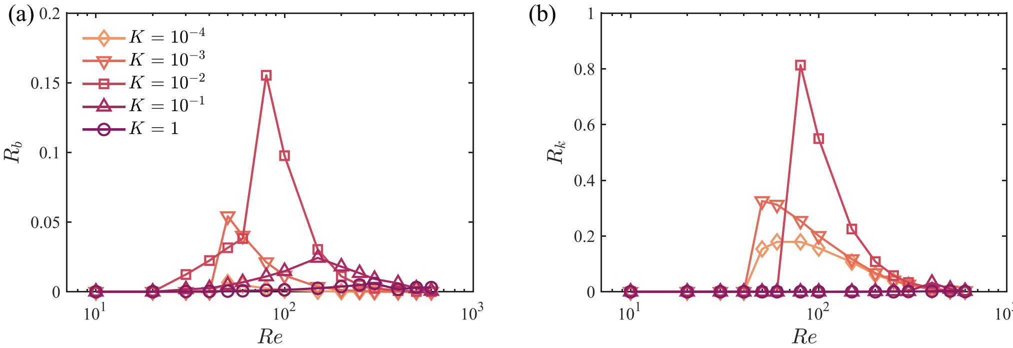

FIG. 15. Conversion ratios from fluid kinetic energy to filament bending energy R_b (a) and to filament translational kinetic energy R_k (b) as functions of Re for various K.

such that $T = 1/f_1$ (see Fig. 4). For static and quasistatic modes, the period T tends to infinity. Consequently, the interacting fluid kinetic energy $E_{k,f}$ becomes unbounded, causing both R_b and R_k to approach zero. It is important to note that for these two modes, which occur at lower Re, the filament's bending and kinetic energies are indeed very small (see Fig. 13). This observation is consistent with the limiting conversion ratios of zero derived from the energy ratio definition.

Figure 15 presents R_b and R_k as functions of Re. For a fixed K, both ratios initially increase and subsequently decrease with increasing Re. At low Re, filament bending deformation and translational speed are minimal, while high Re (corresponding to large inflow speeds) yields relatively substantial fluid kinetic energy. As a result, R_b and R_k approach zero at low and high Re. In contrast, moderate Re values maximize both ratios, with peak values of $R_b = 15.5\%$ and $R_k = 81.3\%$ observed at $K = 10^{-2}$ and $Re = 80$. Notably, R_k significantly exceeds R_b, indicating predominant conversion of fluid kinetic energy to filament kinetic energy.

V. CONCLUDING REMARKS

In this study, the symmetry breaking of flexible filaments free to move laterally within a uniform flow is investigated numerically. It is found that, by extracting energy solely from the surrounding flow, the filaments can achieve sustained lateral motion in certain situations. Five distinct modes, i.e., static, quasistatic, translational, vibrational, and chaotic modes, are identified based on filament motion and flow patterns, and a phase diagram for these modes is presented in the Re-K plane. These modes are quantitatively delineated using the translational Reynolds number (Re_V) and Strouhal number (St). The quasistatic mode occurs exclusively at low K values within a narrow Re range ($Re \approx 40$). At elevated K, this mode disappears and is supplanted by vibrational motion.

Actually, the modal transitions of filaments at different bending stiffnesses K correspond to distinct bifurcation phenomena. For small values of K (e.g., $K = 0.0001$ and 0.001), an increase in the Reynolds number Re causes the filament to transition from a static mode, characterized by zero lateral velocity, to a quasistatic/translational mode, which exhibits a finite lateral velocity. Under different initial perturbations, this quasistatic/translational mode bifurcates into two symmetric branches, with equal velocity magnitudes but opposite directions (see Appendix C). This behavior is a classic example of a supercritical pitchfork bifurcation, wherein the two branches represent two stable fixed points in the phase space [74]. Conversely, for large values of K (e.g., $K \geqslant 0.01$), an increase in Re prompts a transition from the static mode to a vibrational mode, where the mean lateral velocity remains zero. This transition is intimately linked to the onset of vortex shedding. Analogous to the behavior observed in flow past a cylinder, it represents a manifestation of a Hopf bifurcation [2].

Filament reconfiguration and hydrodynamic forces are analyzed in detail. As anticipated, bending deformation and drag increase with inflow velocity. Force decomposition reveals that the normal force (f_n) is approximately uniformly distributed along the filament, while the tangential force (f_τ) is negligible. Utilizing these assumptions, a reduced-order parametrized model is developed to accurately predict equilibrium curvature and filament shape. Furthermore, asymmetric deformation is identified as the primary driver of unidirectional motion.

To elucidate underlying mechanisms, new scaling parameters, i.e., the effective bending stiffness (K_{eff}) and effective Reynolds number (Re_{eff}), are introduced. These parameters enable complete data collapse for filament deformation and force. Detailed energy analysis demonstrates efficient conversion of fluid kinetic energy into filament kinetic and bending energy at moderate Re. Collectively, these results advance fundamental understanding of fluid-flexible structure interactions.

ACKNOWLEDGMENTS

This work was supported by the Natural Science Foundation of China (NSFC) Grants No. 12388101, No. 12502308, No. 12293002, and No. 12293000, the Postdoctoral Fellowship Program of CPSF under Grant No. GZC20241645, and the China Postdoctoral Science Foundation under Grant No. 2025M781800. We thank Dr. M.-F. Xu for useful conversations and J.-Q. Xiong for assistance with the manuscript revision. Numerical computations were performed at the Hefei Advanced Computing Center.

DATA AVAILABILITY

The data supporting this study's findings are available within the article.

APPENDIX A: VERIFICATION OF THE MOVING COMPUTATIONAL DOMAIN

The effect of the MCD is evaluated here. For comparison, additional numerical simulations are conducted using a large fixed computational domain (FCD) spanning $[-15L, 25L]$ in the x-direction and $[-100L, 100L]$ in the y-direction. The extent of the computational domain in the y-direction is sufficiently large to ensure the filament reaches an equilibrium state before approaching the boundaries. Figure 16 presents the time history of the streamwise force F_x and the lateral velocity of the center of mass V for the filament, obtained using both the MCD and FCD for the case with $Re = 100$ and $K = 0.0001$. It can be observed that, despite a certain phase difference, the average values, amplitudes, and frequencies of F_x and V remain unchanged. Therefore, the use of the moving computational domain technique has no impact on the kinematic and dynamic characteristics of the filament in equilibrium.

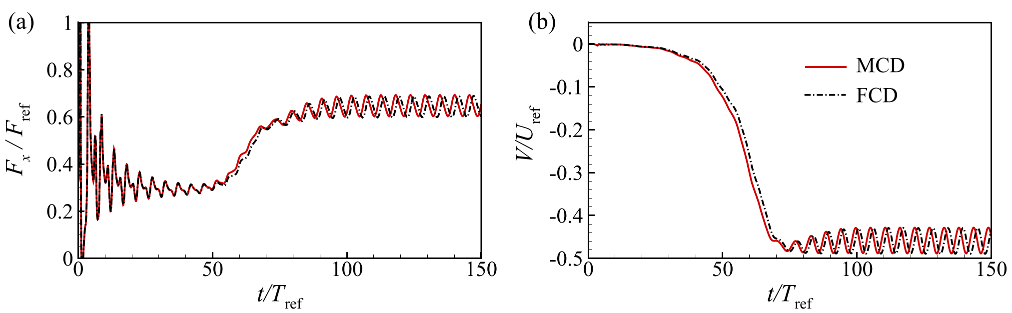

FIG. 16. Comparison of results using MCD and FCD. Time history of (a) the streamwise force F_x and (b) the lateral velocity of the center-of-mass V of the filament are presented. The parameters are $Re = 100$ and $K = 0.0001$.

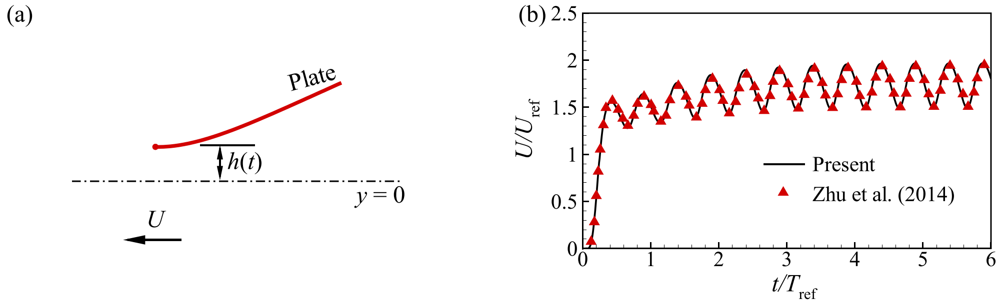

FIG. 17. (a) Schematic diagram of the heaving flexible plate. Here, $h(t)$ is the instantaneous heaving motion prescribed in the leading edge, and U is the instantaneous streamwise velocity of the plate. (b) Validation for the case of a self-propelled heaving plate with the governing parameters: $Re = 200$, $h_0 = 0.5$, $M = 0.2$, $K = 0.8$, and $S = 1000$ [75]. The streamwise velocity of the leading edge as a function of time is presented.

APPENDIX B: VALIDATION FOR THE CASE OF A SELF-PROPELLED HEAVING PLATE

To further validate the numerical method, a self-propelled heaving plate is considered. As shown in Fig. 17(a), the leading edge of the flexible plate is forced to heave in the lateral direction, described as

$$h(t) = h_0 \sin(2\pi f t), \tag{B1}$$

where h_0 and f are the heaving amplitude and frequency, respectively. Similar to the filament in our study, the flexible plate can propel itself forward due to fluid-structure interaction. For the case with $Re = 200$, $h_0 = 0.5$, $M = 0.2$, $K = 0.8$, and $S = 1000$, the streamwise velocity of the leading edge U as a function of time is presented in Fig. 17(b), showing good agreement with that of Zhu *et al.* [75]. This agreement demonstrates that the numerical strategy employed in our study is capable of effectively simulating the motion of flexible plates or filaments.

APPENDIX C: EFFECTS OF THE INITIAL PERTURBATIONS

In the following, the influence of initial perturbations on the system's evolution is examined in detail. While such perturbations can manifest in various forms, we introduce, without loss of generality, a sinusoidal disturbance in the lateral velocity component of the initial flow field. Specifically, the flow field at $t = 0$ is given by

$$\boldsymbol{v}(\boldsymbol{x}, 0) = (U_\infty,\ \beta U_{\mathrm{ref}} \sin(2\pi x/L)), \tag{C1}$$

where β is a dimensionless parameter representing the disturbance intensity. A value of $\beta = 0$ corresponds to an unperturbed initial condition.

Figure 18 presents the time history of the filament's center-of-mass lateral velocity (V) for the four characteristic motion modes (static, quasistatic, translational, and vibrational) under varying initial disturbance intensities β. The results demonstrate that β has a substantial effect on the transient dynamics, significantly altering the time required to reach the equilibrium state for all modes. Notably, with the exception of the static mode Fig. 18(a), the introduction of a finite perturbation ($\beta \neq 0$) considerably reduces this transient period, as exemplified by the vibrational case in Fig. 18(d). While changing the sign of β primarily dictates the direction of the filament's initial motion [e.g., from downward to upward motion in Figs. 18(b) and 18(c)], it does not affect the key statistical characteristics of the final equilibrium state. Quantities such as the magnitude of the mean lateral velocity, the oscillation amplitude of lateral velocity, and the dominant vibration frequency remain invariant with respect to β. Consequently, the introduction of an initial perturbation does not fundamentally alter the emergent motion mode of the filament. These findings further substantiate

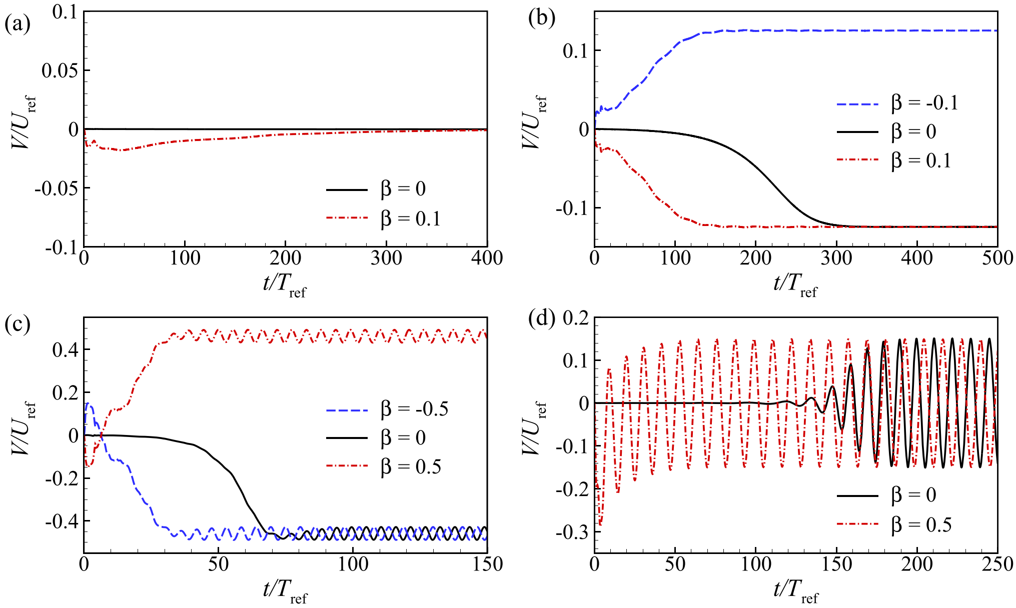

FIG. 18. Time history of lateral velocity of the center-of-mass V of the filament under different initial disturbance intensities β for (a) $Re = 20$, $K = 0.0001$, (b) $Re = 40$, $K = 0.0001$, (c) $Re = 100$, $K = 0.0001$, and (d) $Re = 100$, $K = 0.1$, corresponding to the static, quasistatic, translational, and vibrational modes, respectively.

that the observed symmetry breaking is a consequence of an intrinsic physical instability, rather than being an artifact of numerical asymmetries or specific implementation details.

APPENDIX D: FORCE DECOMPOSITION

In order to establish a simplified model for evaluating the equilibrium configuration of the flexible filament, we first examine the forces acting on it. As shown in Fig. 19, the Lagrangian force $\boldsymbol{f}_s$ exerted by the surrounding fluid on the filament can be decomposed into two components: the normal force $\boldsymbol{f}_n$ (predominantly due to pressure difference across the filament) and the tangential force $\boldsymbol{f}_\tau$ (primarily arising from viscous effects). The definitions of these forces are as follows [45,54,76]:

$$\boldsymbol{f}_s = [-p\boldsymbol{I} + \boldsymbol{T}_\mu] \cdot \boldsymbol{n} = \boldsymbol{f}_n + \boldsymbol{f}_\tau, \tag{D1}$$

$$\boldsymbol{f}_n = (\boldsymbol{f}_s \cdot \boldsymbol{n})\boldsymbol{n} = f_n\boldsymbol{n} = (f_{n,x}, f_{n,y}), \tag{D2}$$

$$\boldsymbol{f}_\tau = (\boldsymbol{f}_s \cdot \boldsymbol{\tau})\boldsymbol{\tau} = f_\tau\boldsymbol{\tau} = (f_{\tau,x}, f_{\tau,y}), \tag{D3}$$

where $\boldsymbol{I}$ is the unit tensor, $\boldsymbol{T}_\mu$ is the viscous stress tensor, f_n and f_τ denote the magnitudes of $\boldsymbol{f}_n$ and $\boldsymbol{f}_\tau$, respectively, $\boldsymbol{\tau}$ is the unit tangential vector directed toward the trailing edge, $\boldsymbol{n}$ is the unit normal vector, and $[\cdot]$ represents the jump in a quantity across the immersed boundary.

Figure 20 presents the distributions of normal and tangential forces (f_n and f_τ) along the filament at various Re for $K = 0.01$. As shown in Fig. 20(a), f_n increases monotonically with inflow velocity (i.e., U_∞ or Re), since the pressure difference across the filament can be scaled as ρU_∞^2 [28,77]. Furthermore, f_n is approximately uniformly distributed along the filament (i.e., $f_n \approx C$), except near the end points. In contrast, f_τ is negligible [see Fig. 20(b)] due to its relatively small magnitude (i.e., $f_\tau \approx 0$).

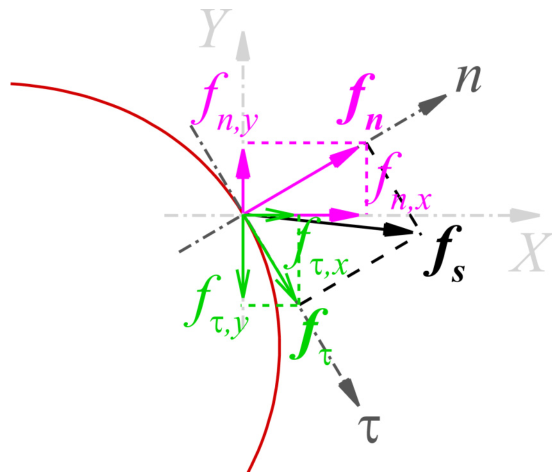

FIG. 19. Schematic diagram of force decomposition. Here, $\boldsymbol{\tau}$ and $\boldsymbol{n}$ denote the local tangential and normal vectors, respectively.

Here, we would like to provide a simple physical rationale for neglecting the tangential force. The magnitude of the total tangential force, defined as $F_\tau = |\int_0^L f_\tau \mathrm{d}s|$, can be approximated by the viscous drag per unit width on a flat plate: $F_\tau \sim 1.33\rho\bar{V}^2 L Re_V^{-1/2}$ [65,72]. In contrast, the total normal force, i.e., $F_n = \int_0^L f_n \mathrm{d}s$, is primarily attributed to the pressure difference, scaling as $F_n \sim \rho U_\infty^2 L$ [65]. Consequently, the ratio of tangential to normal force can be expressed as

$$F_\tau/F_n \sim 1.33\rho\bar{V}^2 L Re_V^{-1/2}/\left(\rho U_\infty^2 L\right) = 1.33\frac{\bar{V}^2}{U_\infty^2} Re_V^{-1/2}. \tag{D4}$$

In the static and vibrational modes, $F_\tau = 0$ because $\bar{V} = 0$. For other modes where $\bar{V} \neq 0$, $\bar{V}$, and U_∞ are typically of comparable magnitude, with $\bar{V} \sim U_\infty$ in most cases (see Fig. 7). Thus, Eq. (D4) reduces to

$$F_\tau/F_n \sim Re_V^{-1/2}. \tag{D5}$$

Notably, in cases involving lateral translation, Re_V is significantly greater than unity (see Fig. 7). Consequently, $F_\tau/F_n \ll 1$, meaning that F_τ is sufficiently small to be neglected.

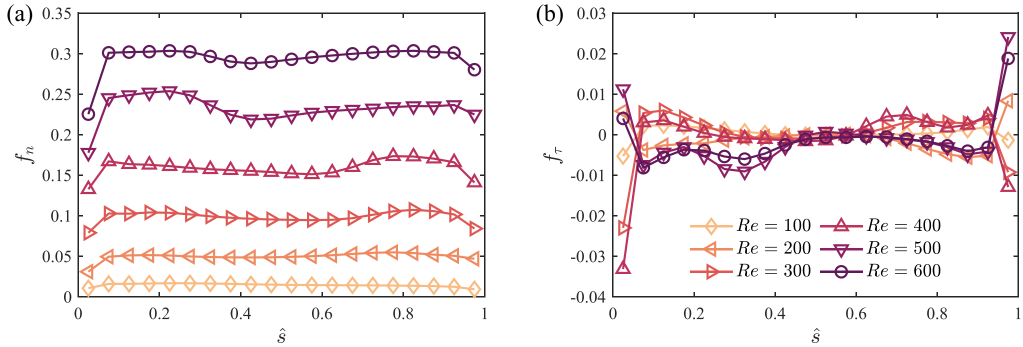

FIG. 20. Distributions of (a) normal force f_n and (b) tangential force f_τ along the filament for various Re with $K = 0.01$.

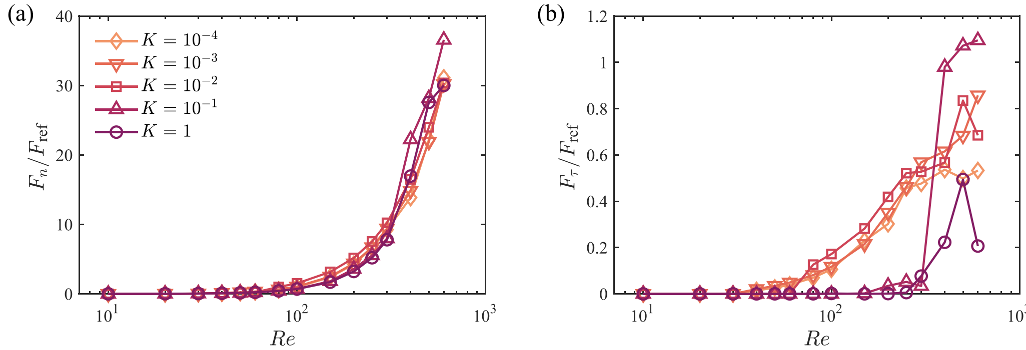

FIG. 21. (a) The total normal force F_n and (b) total tangential force F_τ on the filament as functions of *Re* for various K.

To confirm Eq. (D5), Fig. 21 presents the total normal force F_n and total tangential force F_τ on the filament as functions of *Re* for various K. In all cases, F_τ is observed to be at least one order of magnitude smaller than F_n, consistent with the scaling analysis above. Hence, neglecting the tangential force is a reasonable assumption. These approximations, namely, $f_n \approx C$ and $f_\tau \approx 0$, form the basis of the reduced-order parametrized model for flexible filaments developed in Sec. IV B.

[1] J. Crawford and E. Knobloch, Symmetry and symmetry-breaking bifurcations in fluid dynamics, Annu. Rev. Fluid Mech. **23**, 341 (1991).

[2] C. Williamson, Vortex dynamics in the cylinder wake, Annu. Rev. Fluid Mech. **28**, 477 (1996).

[3] P. Matharu, A. Hazel, and M. Heil, Spatio-temporal symmetry breaking in the flow past an oscillating cylinder, J. Fluid Mech. **918**, A42 (2021).

[4] R. Averitt, Dynamics of broken symmetry, Nat. Phys. **6**, 639 (2010).

[5] S. Bagheri, A. Mazzino, and A. Bottaro, Spontaneous symmetry breaking of a hinged flapping filament generates lift, Phys. Rev. Lett. **109**, 154502 (2012).

[6] U. Lacis, N. Brosse, F. Ingremeau, A. Mazzino, F. Lundell, H. Kellay, and S. Bagheri, Passive appendages generate drift through symmetry breaking, Nat. Commun. **5**, 5310 (2014).

[7] J. Deng, X. Mao, and L. Brandt, Symmetry breaking of tail-clamped filaments in Stokes flow, Phys. Rev. Lett. **126**, 124501 (2021).

[8] R. Cobos, A. Khair, and O. Schnitzer, Spontaneous locomotion of a symmetric squirmer, J. Fluid Mech. **983**, R3 (2024).

[9] O. Williams and A. Smits, Asymmetries in nominally symmetric flows, Annu. Rev. Fluid Mech. **57**, 35 (2025).

[10] N. Vandenberghe, J. Zhang, and S. Childress, Symmetry breaking leads to forward flapping flight, J. Fluid Mech. **506**, 147 (2004).

[11] S. Alben and M. Shelley, Coherent locomotion as an attracting state for a free flapping body, Proc. Natl. Acad. Sci. USA **102**, 11163 (2005).

[12] N. Vandenberghe, S. Childress, and J. Zhang, On unidirectional flight of a free flapping wing, Phys. Fluids **18**, 014102 (2006).

[13] X.-Y. Lu and Q. Liao, Dynamic responses of a two-dimensional flapping foil motion, Phys. Fluids **18**, 098104 (2006).

[14] X. Zhang, S. Ni, S. Wang, and G. He, Effects of geometric shape on the hydrodynamics of a self-propelled flapping foil, Phys. Fluids **21**, 103302 (2009).

[15] J. Deng and C. Caulfield, Dependence on aspect ratio of symmetry breaking for oscillating foils: Implications for flapping flight, J. Fluid Mech. **787**, 16 (2016).
[16] L. Benetti Ramos, O. Marquet, M. Bergmann, and A. Iollo, Fluid–solid Floquet stability analysis of self-propelled heaving foils, J. Fluid Mech. **910**, A28 (2021).
[17] X. Zhu, G. He, and X. Zhang, How flexibility affects the wake symmetry properties of a self-propelled plunging foil, J. Fluid Mech. **751**, 164 (2014).
[18] K. Liu and H. Huang, Wake transition of an unconstrained self-propelled flexible flapping plate, Phys. Rev. Fluids **9**, 033102 (2024).
[19] R. Godoy-Diana, J.-L. Aider, and J. Wesfreid, Transitions in the wake of a flapping foil, Phys. Rev. E **77**, 016308 (2008).
[20] A. Andersen, T. Bohr, T. Schnipper, and J. H. Walther, Wake structure and thrust generation of a flapping foil in two-dimensional flow, J. Fluid Mech. **812**, R4 (2017).
[21] D. Jallas, O. Marquet, and D. Fabre, Linear and nonlinear perturbation analysis of the symmetry breaking in time-periodic propulsive wakes, Phys. Rev. E **95**, 063111 (2017).
[22] Z.-R. Peng, Y. Sun, D. Yang, Y. Xiong, L. Wang, and L. Wang, Scaling laws for drag-to-thrust transition and propulsive performance in pitching flexible plates, J. Fluid Mech. **941**, R2 (2022).
[23] R. Godoy-Diana, C. Marais, J.-L. Aider, and J. Wesfreid, A model for the symmetry breaking of the reverse Bénard–von Kármán vortex street produced by a flapping foil, J. Fluid Mech. **622**, 23 (2009).
[24] C. Marais, B. Thiria, J. Wesfreid, and R. Godoy-Diana, Stabilizing effect of flexibility in the wake of a flapping foil, J. Fluid Mech. **710**, 659 (2012).
[25] L.-B. Jia, F. Li, X.-Z. Yin, and X.-Y. Yin, Coupling modes between two flapping filaments, J. Fluid Mech. **581**, 199 (2007).
[26] L.-B. Jia and X.-Z. Yin, Passive oscillations of two tandem flexible filaments in a flowing soap film, Phys. Rev. Lett. **100**, 228104 (2008).
[27] C. Eloy, R. Lagrange, C. Souilliez, and L. Schouveiler, Aeroelastic instability of cantilevered flexible plates in uniform flow, J. Fluid Mech. **611**, 97 (2008).
[28] L. Ristroph and J. Zhang, Anomalous hydrodynamic drafting of interacting flapping flags, Phys. Rev. Lett. **101**, 194502 (2008).
[29] M. Shelley and J. Zhang, Flapping and bending bodies interacting with fluid flows, Annu. Rev. Fluid Mech. **43**, 449 (2011).
[30] J. Zhang, S. Childress, A. Libchaber, and M. Shelley, Flexible filaments in a flowing soap film as a model for one-dimensional flags in a two-dimensional wind, Nature (London) **408**, 835 (2000).
[31] M. Shelley, N. Vandenberghe, and J. Zhang, Heavy flags undergo spontaneous oscillations in flowing water, Phys. Rev. Lett. **94**, 094302 (2005).
[32] B. Connell and D. Yue, Flapping dynamics of a flag in a uniform stream, J. Fluid Mech. **581**, 33 (2007).
[33] S. Alben and M. Shelley, Flapping states of a flag in an inviscid fluid: Bistability and the transition to chaos, Phys. Rev. Lett. **100**, 074301 (2008).
[34] D. Kim, J. Cossé, C. Huertas Cerdeira, and M. Gharib, Flapping dynamics of an inverted flag, J. Fluid Mech. **736**, R1 (2013).
[35] H. Huang, H. Wei, and X.-Y. Lu, Coupling performance of tandem flexible inverted flags in a uniform flow, J. Fluid Mech. **837**, 461 (2018).
[36] Y. Yu, Y. Liu, and X. Amandolese, A review on fluid-induced flag vibrations, Appl. Mech. Rev. **71**, 010801 (2019).
[37] M. Tavallaeinejad, M. Païdoussis, M. Legrand, and M. Kheiri, Instability and the post-critical behaviour of two-dimensional inverted flags in axial flow, J. Fluid Mech. **890**, A14 (2020).
[38] C. Tang, N. Liu, and X.-Y. Lu, Dynamics of an inverted flexible plate in a uniform flow, Phys. Fluids **27**, 073601 (2015).
[39] J. Sader, J. Cossé, D. Kim, B. Fan, and M. Gharib, Large-amplitude flapping of an inverted flag in a uniform steady flow–a vortex-induced vibration, J. Fluid Mech. **793**, 524 (2016).
[40] C. Huertas-Cerdeira, A. Goza, J. Sader, T. Colonius, and M. Gharib, Dynamics of an inverted cantilever plate at moderate angle of attack, J. Fluid Mech. **909**, A20 (2021).

[41] K. Shoele and R. Mittal, Energy harvesting by flow-induced flutter in a simple model of an inverted piezoelectric flag, J. Fluid Mech. **790**, 582 (2016).
[42] H. Zhang, Y. Zhao, P. Wang, B. Wen, X. Tian, and H. Liu, Numerical simulations on the flow past a flexible filament with two fixed ends at a low Reynolds number, J. Fluid Mech. **1009**, A5 (2025).
[43] L. Zhu and C. Peskin, Simulation of a flapping flexible filament in a flowing soap film by the immersed boundary method, J. Comput. Phys. **179**, 452 (2002).
[44] R.-N. Hua, L. Zhu, and X.-Y. Lu, Locomotion of a flapping flexible plate, Phys. Fluids **25**, 121901 (2013).
[45] K. Liu and H. Huang, Dynamics of weighted flexible ribbons in a uniform flow, J. Fluid Mech. **990**, A11 (2024).
[46] S. Chen and G. Doolen, Lattice Boltzmann method for fluid flows, Annu. Rev. Fluid Mech. **30**, 329 (1998).
[47] J. Doyle, *Nonlinear Analysis of Thin-Walled Structures: Statics, Dynamics, and Stability* (Springer, New York, 2001).
[48] R. Mittal and G. Iaccarino, Immersed boundary methods, Annu. Rev. Fluid Mech. **37**, 239 (2005).
[49] W. Huang, S. Shin, and H. Sung, Simulation of flexible filaments in a uniform flow by the immersed boundary method, J. Comput. Phys. **226**, 2206 (2007).
[50] R.-N. Hua, L. Zhu, and X.-Y. Lu, Dynamics of fluid flow over a circular flexible plate, J. Fluid Mech. **759**, 56 (2014).
[51] C. Zhang, H. Huang, and X.-Y. Lu, Effect of trailing-edge shape on the self-propulsive performance of heaving flexible plates, J. Fluid Mech. **887**, A7 (2020).
[52] M.-C. Lai and C. Peskin, An immersed boundary method with formal second-order accuracy and reduced numerical viscosity, J. Comput. Phys. **160**, 705 (2000).
[53] C. S. Peskin, The immersed boundary method, Acta Numer. **11**, 479 (2002).
[54] K. Liu, X. Liu, and H. Huang, Scaling the self-propulsive performance of pitching and heaving flexible plates, J. Fluid Mech. **936**, A9 (2022).
[55] L. Zhu, Viscous flow past a flexible fibre tethered at its centre point: Vortex shedding, J. Fluid Mech. **587**, 217 (2007).
[56] L. Zhu, Scaling laws for drag of a compliant body in an incompressible viscous flow, J. Fluid Mech. **607**, 387 (2008).
[57] W. Huang and H. Sung, Three-dimensional simulation of a flapping flag in a uniform flow, J. Fluid Mech. **653**, 301 (2010).
[58] Y. Sun, Z. Peng, D. Yang, Y. Xiong, L. Wang, and L. Wang, Dynamics of a rigid-flexible coupling system in a uniform flow, J. Fluid Mech. **943**, A44 (2022).
[59] See Supplemental Material at http://link.aps.org/supplemental/10.1103/5w11-6yc4 for the Supplemental Movies and corresponding descriptions.
[60] P. Bintein, H. Bense, C. Clanet, and D. Quéré, Self-propelling droplets on fibres subject to a crosswind, Nat. Phys. **15**, 1027 (2019).
[61] C. Williamson and R. Govardhan, Vortex-induced vibrations, Annu. Rev. Fluid Mech. **36**, 413 (2004).
[62] T. Sarpkaya, A critical review of the intrinsic nature of vortex-induced vibrations, J. Fluids Struct. **19**, 389 (2004).
[63] M. Raissi, Z. Wang, M. Triantafyllou, and G. Karniadakis, Deep learning of vortex-induced vibrations, J. Fluid Mech. **861**, 119 (2019).
[64] P. Han, E. de Langre, M. Thompson, K. Hourigan, and J. Zhao, Vortex-induced vibration forever even with high structural damping, J. Fluid Mech. **962**, A13 (2023).
[65] G. Batchelor, *An Introduction to Fluid Dynamics* (Cambridge University Press, 1967).
[66] S. Vogel, Drag and reconfiguration of broad leaves in high winds, J. Expl. Bot. **40**, 941 (1989).
[67] F. Gosselin, E. de Langre, and B. Machado-Almeida, Drag reduction of flexible plates by reconfiguration, J. Fluid Mech. **650**, 319 (2010).
[68] T. Barois and E. de Langre, Flexible body with drag independent of the flow velocity, J. Fluid Mech. **735**, R2 (2013).
[69] L. Schouveiler and C. Eloy, Flow-induced draping, Phys. Rev. Lett. **111**, 064301 (2013).
[70] L. Schouveiler and A. Boudaoud, The rolling up of sheets in a steady flow, J. Fluid Mech. **563**, 71 (2006).

[71] M.-F. Xu and Y.-L. Yu, Effects of body stiffness on propulsion during fish self-propelled swimming, Phys. Fluids **35**, 071905 (2023).

[72] S. Alben, M. Shelley, and J. Zhang, Drag reduction through self-similar bending of a flexible body, Nature (London) **420**, 479 (2002).

[73] A. Smits, Undulatory and oscillatory swimming, J. Fluid Mech. **874**, P1 (2019).

[74] S. Strogatz, Nonlinear dynamics and chaos: With applications to physics, *Biology, Chemistry, and Engineering* (CRC Press, 2018).

[75] X. Zhu, G. He, and X. Zhang, Flow-mediated interactions between two self-propelled flapping filaments in tandem configuration, Phys. Rev. Lett. **113**, 238105 (2014).

[76] Z.-R. Peng, H. Huang, and X.-Y. Lu, Collective locomotion of two closely spaced self-propelled flapping plates, J. Fluid Mech. **849**, 1068 (2018).

[77] S. Gao, S. Pan, H. Wang, and X. Tian, Shape deformation and drag variation of a coupled rigid-flexible system in a flowing soap film, Phys. Rev. Lett. **125**, 034502 (2020).